Supporting Information

Local charge polarization by introducing cayanamide group and sulfur dopant with accelerated exciton dissociation and promoted charge separation for improving CO_2 photoreduction performance

Yanrui Li,[*a] Bozhan Li,[a] Xiang Gao,[b] Linda Wang,[a] Xuehao Li,[a] Ruyu Guo[a]

a. College of Materials Science and Engineering, Xi'an University of Science and Technology, Xi'an, 710054, China. E-mail:liyanrui91@xust.edu.cn

b. College of Geology and Environment, Xi'an University of Science and Technology, Xi'an 710054, China.

Experimental Section

Chemicals and Materials

Melamine (MA), Potassium thiocyanate (KSCN) and Thiocarbamide (CH_4N_2S) were purchased from Sinopharm Chemical Reagent Co., Ltd (PR China), which were utilized without further purification.

Synthesis of graphitic carbon nitride (GCN)

The GCN was synthesized by the thermal polycondensation method. For details, 20 g of melamine was put into a crucible with a lid and then put into a tube furnace, which was heat to 550 ℃ with a rate of 5 ℃/min, and held under Ar atmosphere for 4 h. After cooling down to room temperature, the bulk was roundly ground into powder for further utilization.

Characterization

X-ray diffraction (XRD) patterns of the samples were obtained over the diffraction angle (2^{θ}) of 5-60°on a MiniFlex 600 (Rigaku, Japan) with Cu-Kα radiation. Fourier transform infrared (FTIR) spectra were acquired on a Bruker Tensor Ⅱ spectrometer with KBr pellet. Transmission electron microscopy (TEM) images and scanning electron-microscopy (SEM) with element mapping analyses were conducted on transmission electron microscope (Tecnai G2 F30) and transmission electron microscope (JSM-7800F, JEOL), respectively. X-ray photoelectron spectroscopy (XPS) examinations were carried out on a PHI-1600 Xray photoelectron spectrometer using Al Ka radiation. ^{13}C solid-state nuclear magnetic resonance (NMR) spectra were conducted on cross-polarization (CP) magic-angle spinning (MAS) sequence mode (JNM-ECZ400R/S1, JEOL). The UV-Vis DRS spectrum was measured Shimadzu PE lambda 750 equipped with an integrating sphere, with solid $BaSO_4$ powder as the reference standard. Photoluminescence (PL) spectra were performed on a Shimadzu RF-6000 spectrometer with an excitation wavelength of 370 nm. Temperature-dependent PL spectra on a Fluoromax-4 spectrophotometer equipped with a cryo-77 cryogenic liquid nitrogen thermostat was utilized to measure the exciton binding energy (E_b) by the equation (1)[1]:

$$I(T) = I_0/(1 + A \exp(-E_b/k_BT)) \quad (1)$$

I(T) was the normalized PL intensity at given temperature T, I_0 was the PL intensity at 0K, k_B was the Boltzmann constant and A was the constant related to the density of the nonradiative recombination centers.

Electrochemical characterization.

Electrochemical workstation (CHI760E, ChenHua, China) equipped with the standard three-electrode system was utilized to carry out the electrochemical measurements, in which Pt as the counter electrode, Ag/AgCl electrode as the reference electrode catalyst-coated FTO conductive glass as the working electrode. Additionally, the as-prepared catalysts (5 mg) dissolved in the mixed solution of 20 µL Nafion solution, 400 µL ethanol and 100 µL deionized water were dispersed on FTO conductive glass, which was then dried overnight to obtain working electrode. 0.2 M $NaSO_4$ solution was employed as electrolyte. Mott-Schottky (M-S) plots of as-prepared photocatalysts were recorded at 500, 1000 and 1500 Hz under dark condition. The photocurrent measurement was recorded with a 300 W xenon lamp (PLS-SXE300D). Electrochemical impedance spectroscopy (EIS) plots were carried out with the frequency sweep range of 100-10^6 Hz and the amplitude 5 mV.

Computational Methods

Density functional theory (DFT) calculations were performed through the Cambridge Sequential Total Energy Package (CASTEP) code using the generalized gradient approximation (GGA) and Perdew-Burke-Ernzerhof (PBE) functional[2]. The accurate density of electronic state was calculated by using the plane wave cutoff energy of 435 eV and the *k*-point sets of $1 \times 2 \times 1$. In addition, the energy tolerance and force tolerance were considered as 2×10^{-5} eV·atom^{-1} and 0.05 eV·Å^{-1}, respectively. In order to avoid interactions between the periodic images, a vacuum layer of 10 Å was utilized. The adsorption energy (E_a) of the adsorbates in CO_2 reduction could be calculated by equation 2 as following equation (2)[3]:

$$E_a = E_R^* - (E_R + E^*) \quad (2)$$

Where E_R^* was the total energy of an adsorbate (R) adsorbed on the surface (*) and E_R and E^* are the energies of the single adsorbate and clean surface, respectively.

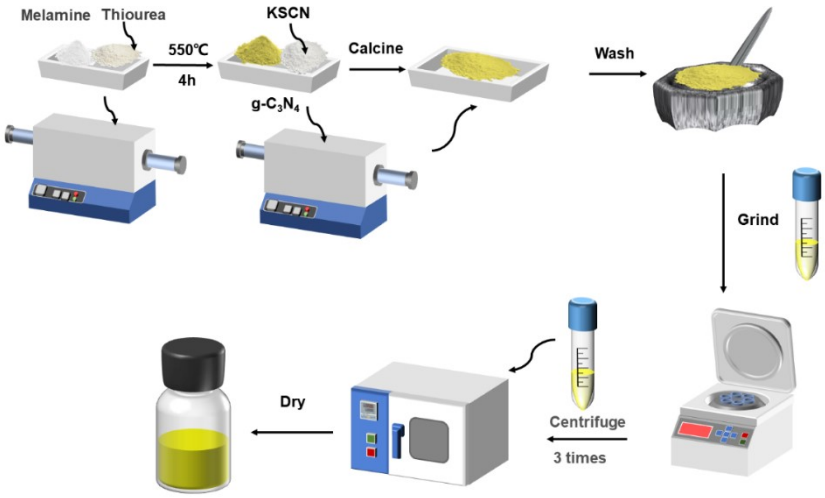

Scheme S1. Schemed fabrication process for SCN-x.

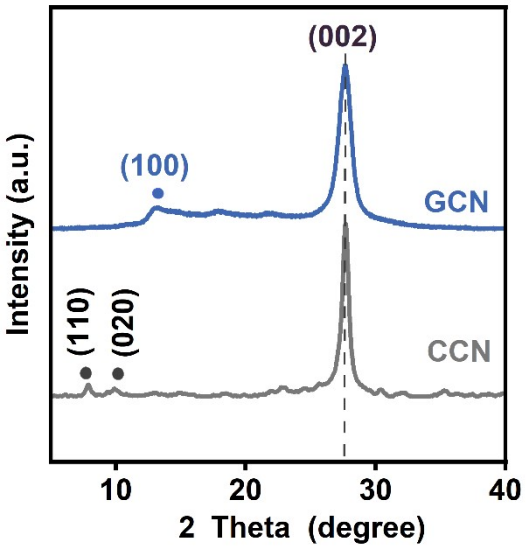

Figure S1. XRD patterns of GCN and CCN.

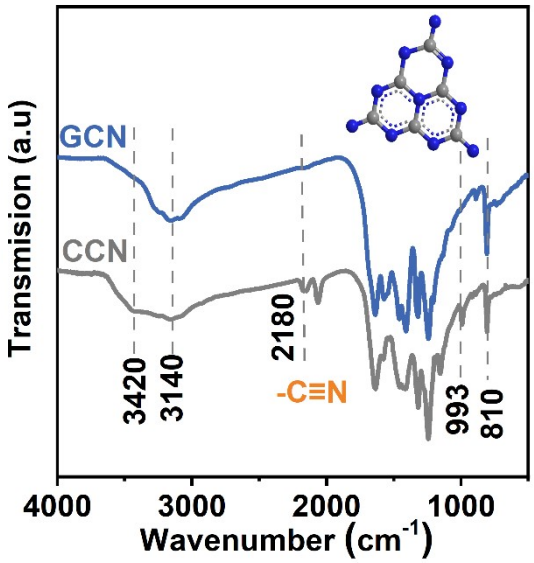

Figure S2. FT-IR spectrum of GCN and CCN.

As illustrated in Figure S3, there was no obvious change on the morphology of SCN-0.5 after introducing S dopant in contract to CCN.

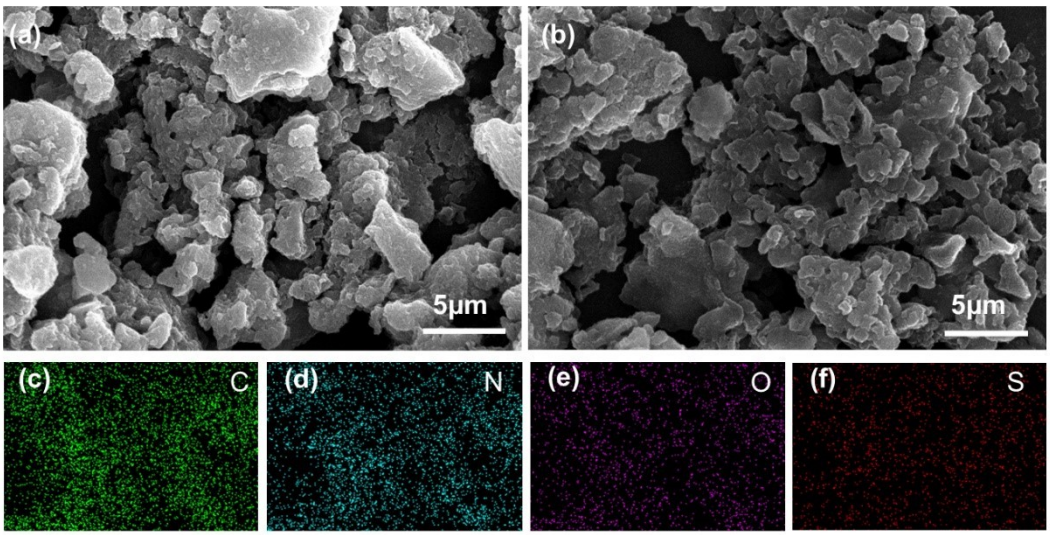

Figure S3. SEM pattern of sample a) CCN, b) SCN-0.5 and SEM-mapping images of c) C, d) N, e) O and f) S of SCN-0.5.

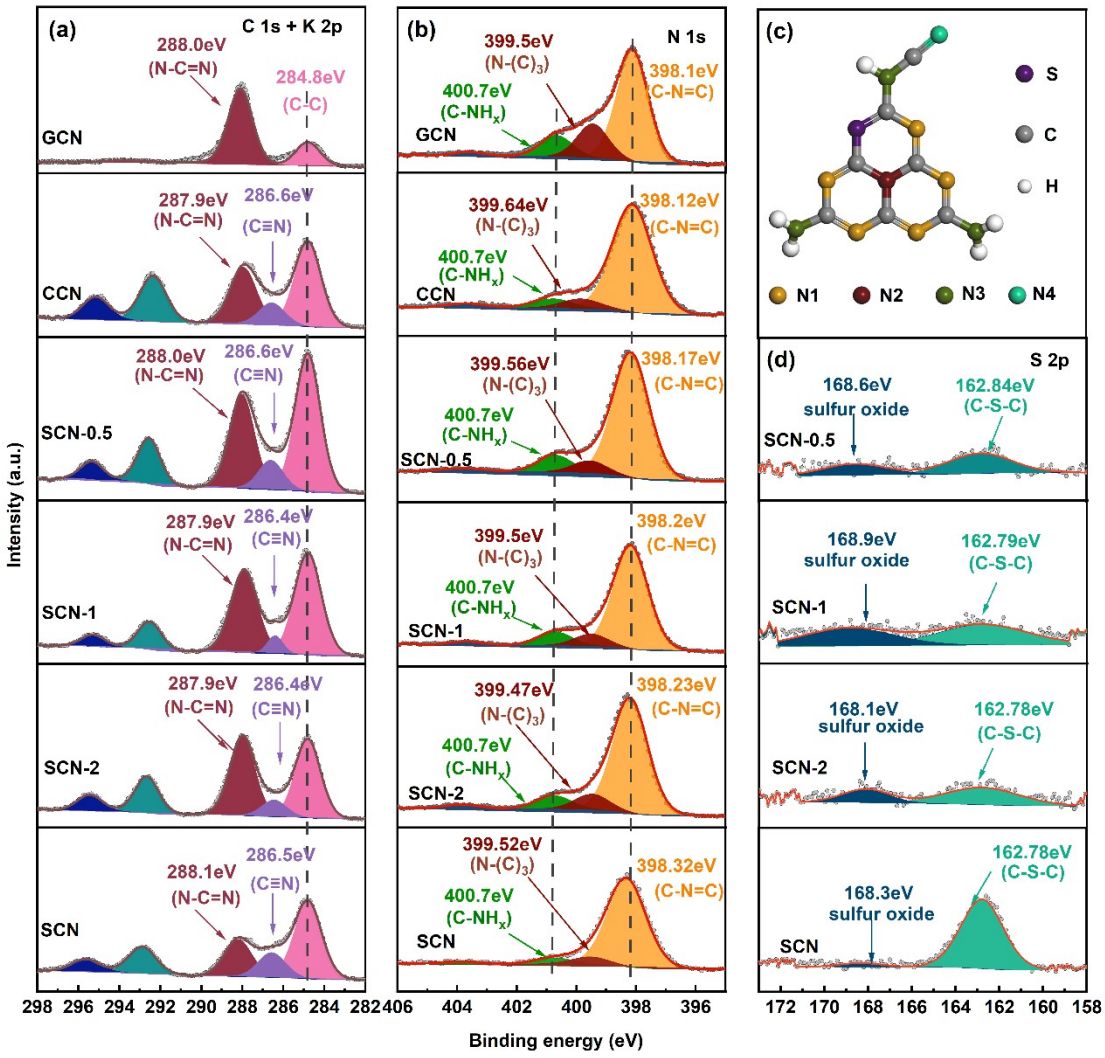

Figure S4. XPS spectra of a) C 1s and K 2p, b) N 1s and d) S 2p for GCN, CCN, and SCN-x. c) Schematic illustration for -CN groups and S dopant in heptazine conjugate ring.

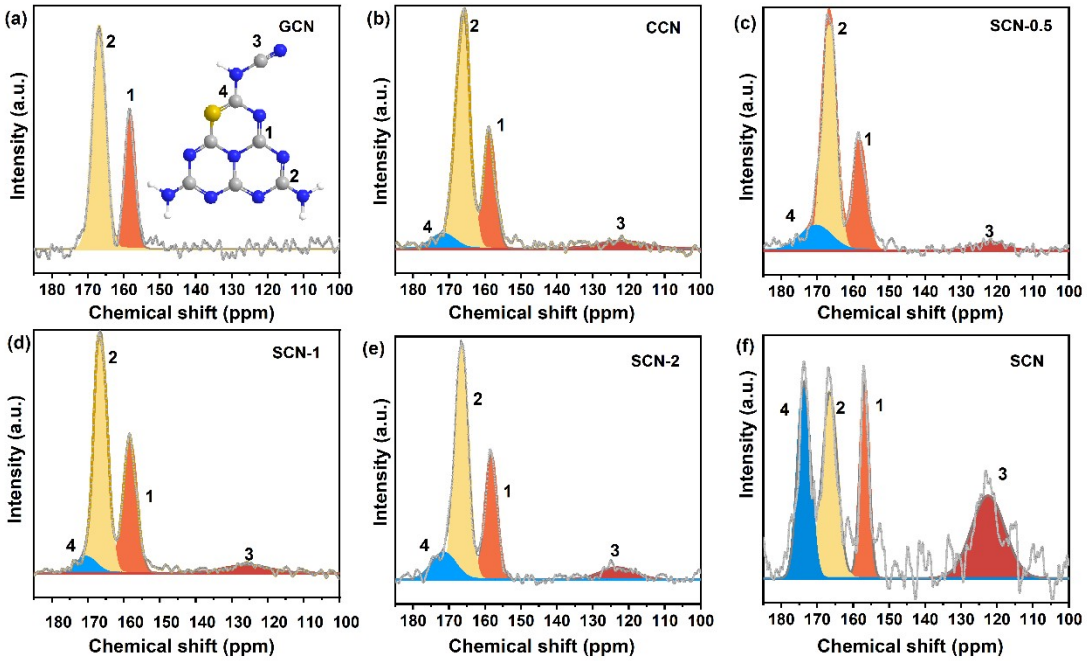

Figure S5. Solid-state ^{13}C NMR spectra for a) GCN, b) CCN, c) SCN-0.5, d) SCN-1, e) SCN-2 and f) SCN.

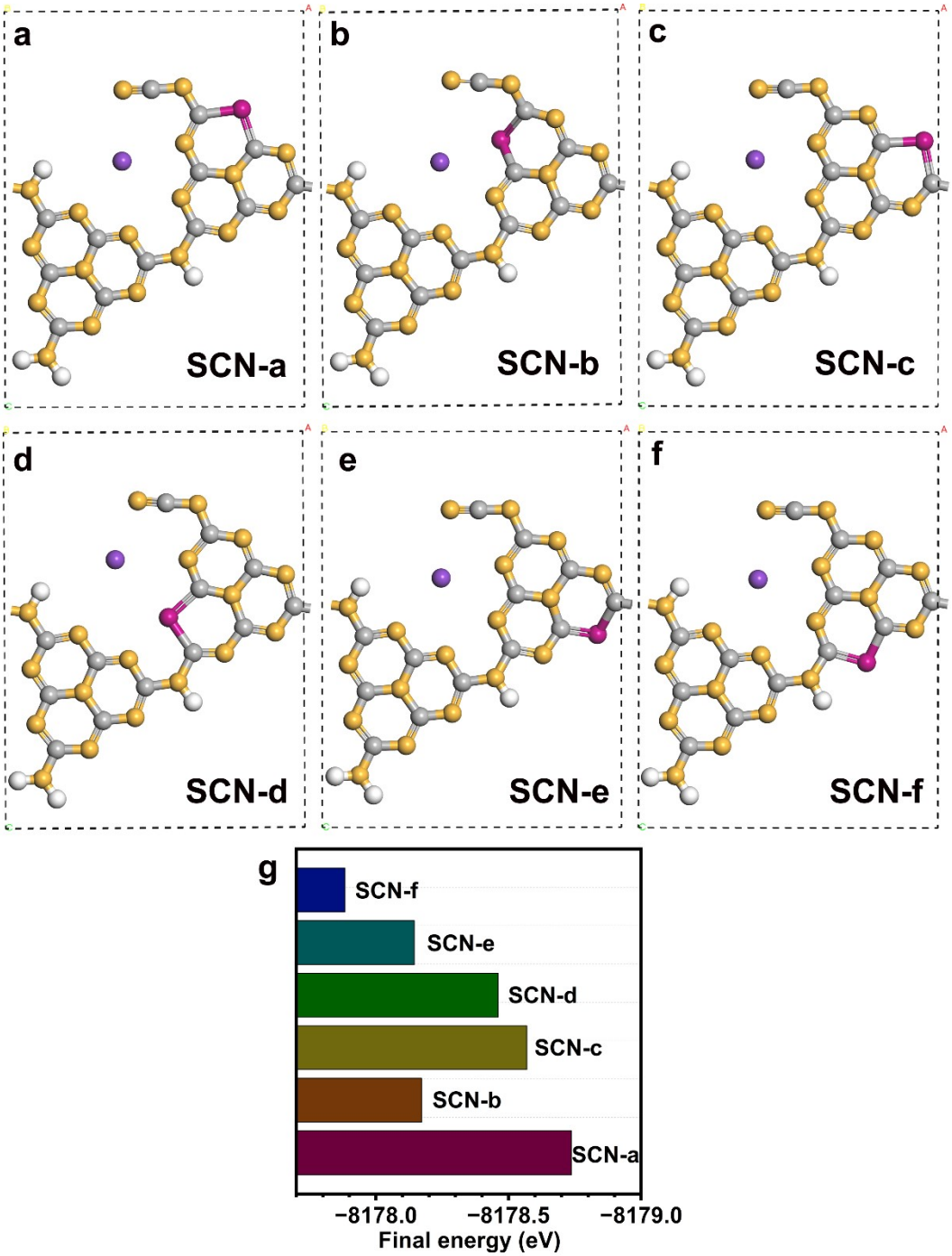

Figure S6. a-f) Six models of N1 replaced by S dopant. g) The formation energy of S dopant replacement models.

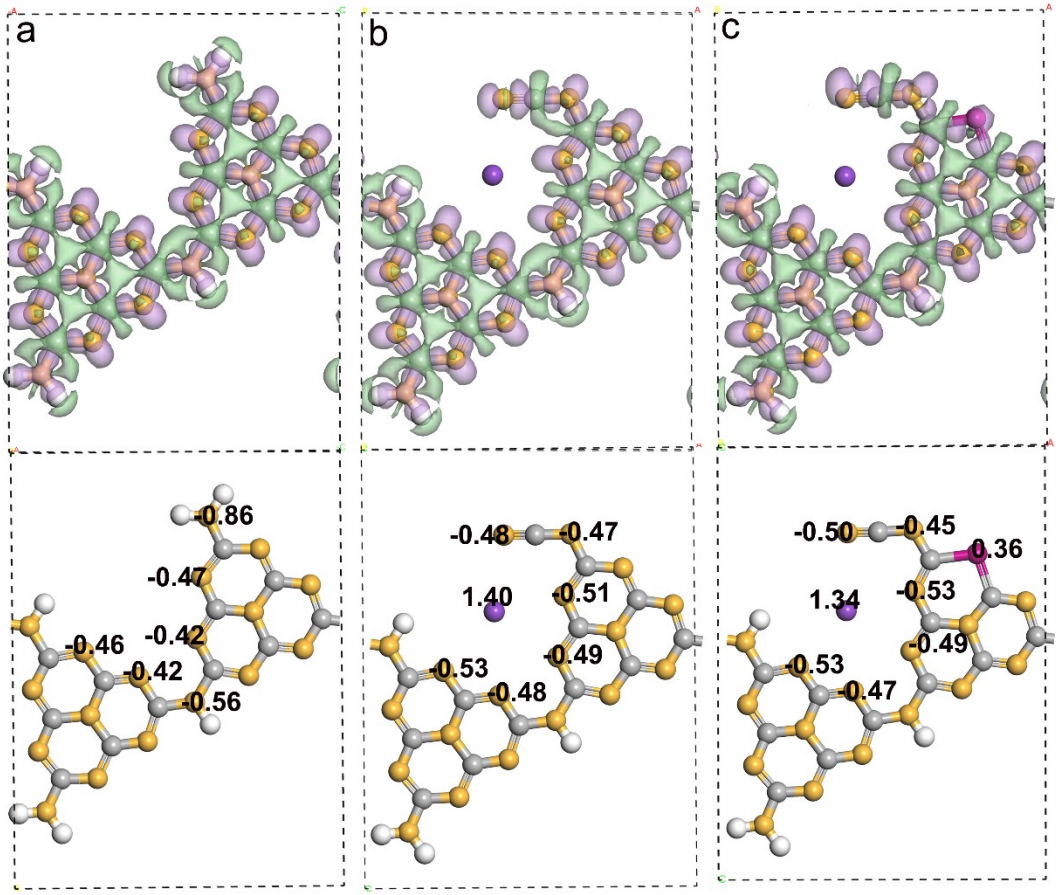

Figure S7. Charge density difference and corresponding bard charge for a) GCN, b) CCN and c) SCN.

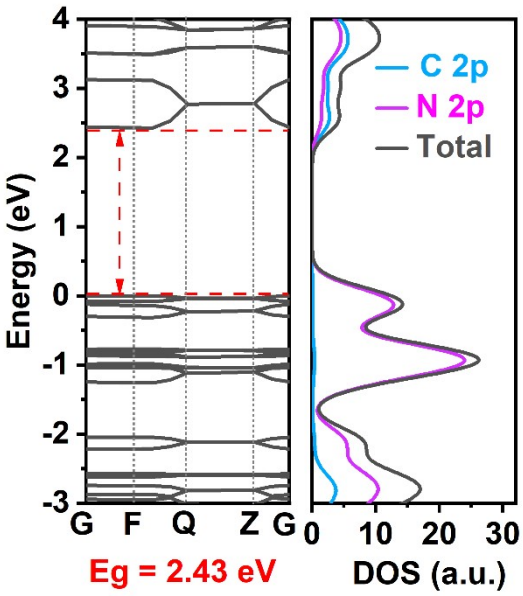

Figure S8. DFT calculated band structure (left) and corresponding density of states (right) for GCN.

The flat-band potentials of GCN, CCN and SCN-x were detected from Mott-Schottky (M-S) plots to be -0.91 V, -0.63 V, -0.88 V, -0.98 V, -1.09V, and -0.93 V (vs. Ag/AgCl), which were equivalent to -0.71 V, -0.43 V, -0.68 V, -0.78 V, -0.89 V, and -0.73 V versus the normal hydrogen electrode (vs. NHE), respectively, according to equation of $E_{NHE} = E_{Ag/AgCl} + 0.197$ V [4] . Generally, the conduction band (CB) minimum is ~0.2 V more negative than the flat-band potential[5]. Therefore, the CB of PCN, CCN, and CCN aerogels could be calculated to be -0.91 V, -0.63 V, -0.88 V, -0.98 V, -1.09 V, and -0.93 V (vs. NHE), respectively.

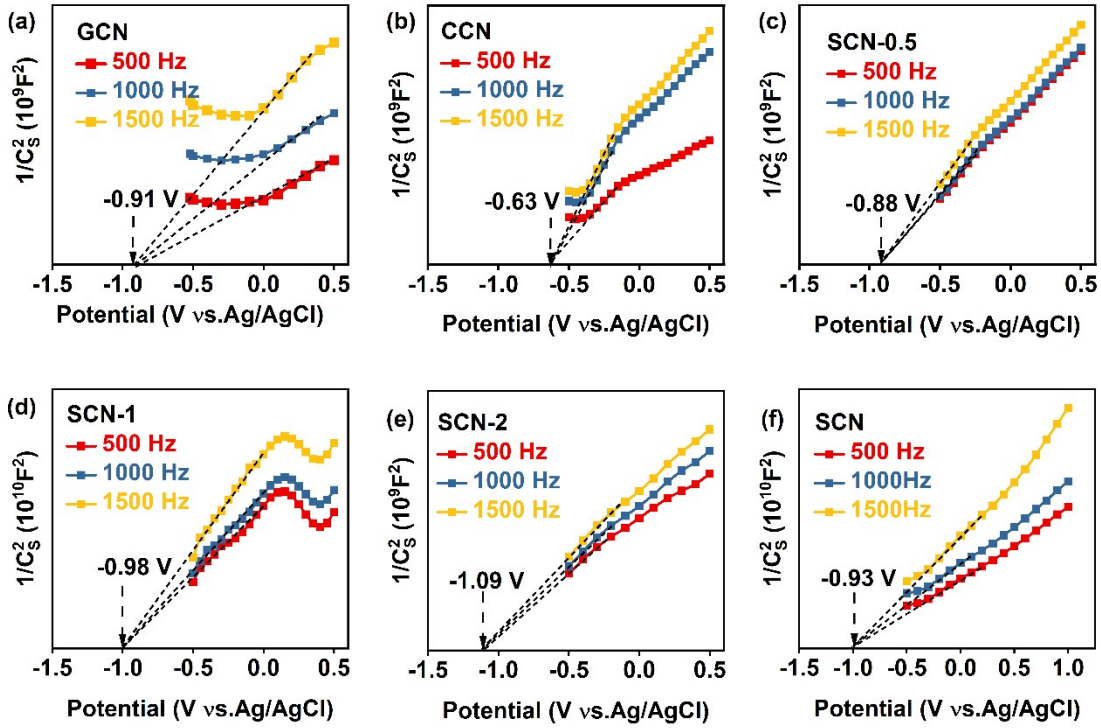

Figure S9. Mott-Schottky (M-S) plots of a) GCN, b) CCN, c) SCN-0.5, d) SCN-1, e) SCN-2, f) SCN.

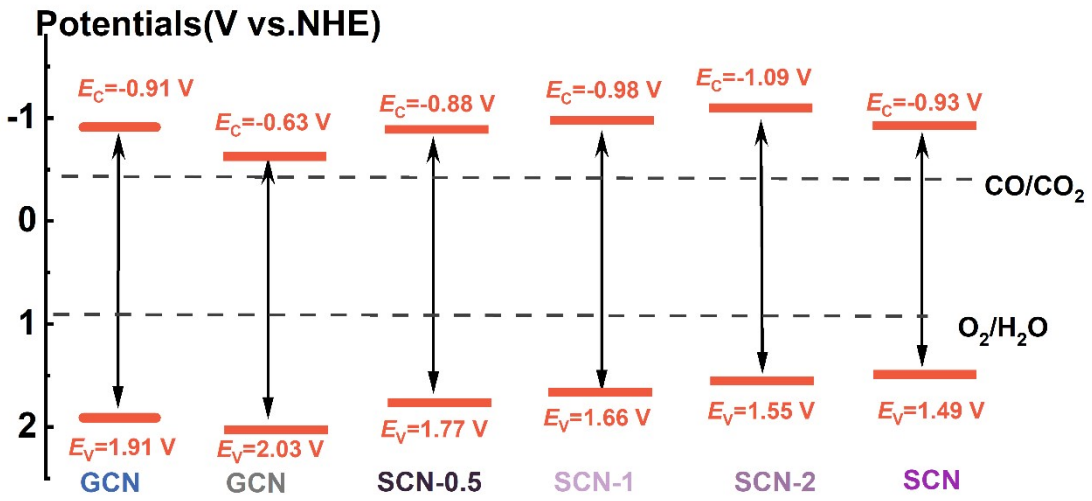

Figure S10. Band structure diagrams of GCN, CCN and SCN-x.

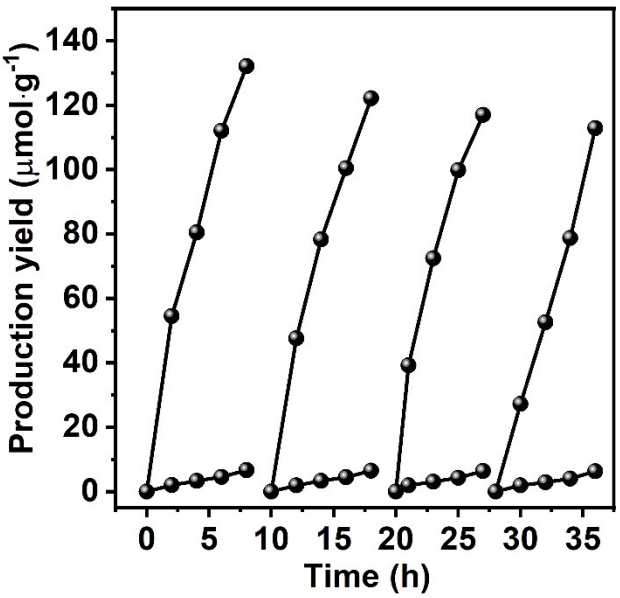

Figure S11. Recycle photocatalytic CO_2 reduction over SCN-x.

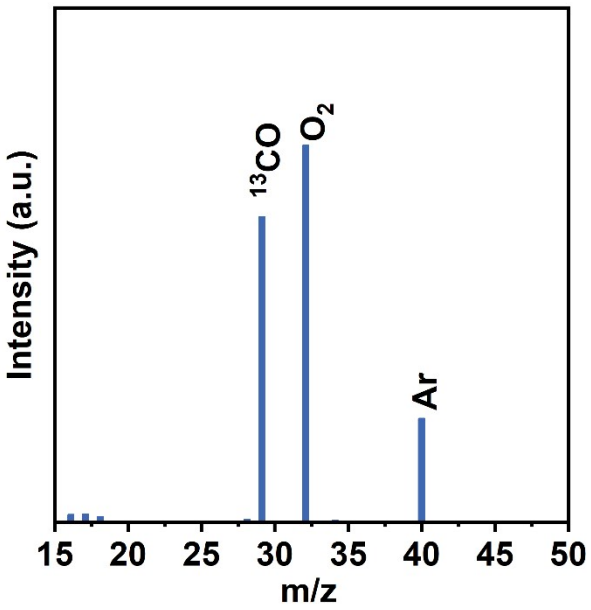

Figure S12. Isotopic measurement of photocatalytic CO_2 reduction using $^{13}CO_2$ as the carbon source.

As illustrated in Figure S13, the CO_2 adsorption curve for GCN exhibited slight rise than CCN in the high-pressure range, which was due to the electrons-accumulated -CN groups favorable for CO_2 adsorption. After introducing S dopant, the curves of SCN-x displayed significant increase than GCN and CCN in both high and low pressure range, attributed to the further enhanced electron density of -CN groups via the charge distribution induced by S dopant. Above phenomenon was consistent with the calculation results of charge density difference of CO_2 adsorption (Figure 5b) and strongly confirmed that SCN-x obtained a stronger ability of CO_2 adsorption than GCN and CCN.

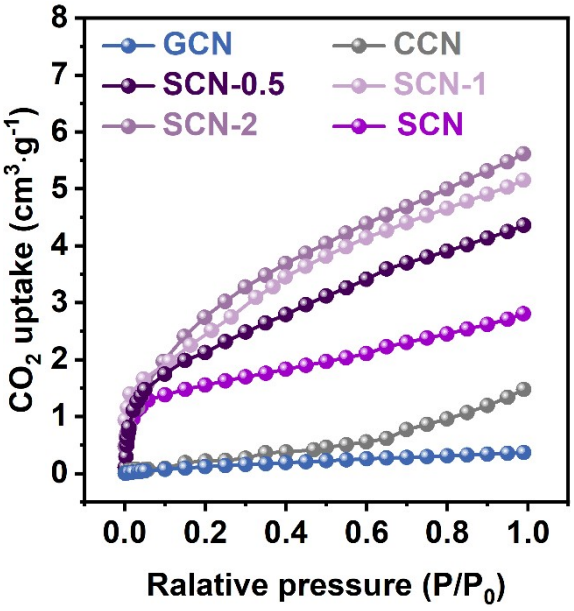

Figure S13. CO_2 gas absorption isotherms of GCN, CCN and SCN-x.

Table S1. The full width at half maxima (FWHM) values and *d*-spacing of the (002) diffraction peak of GCN, CCN and SCN-x estimated by XRD results.

XRD	GCN	CCN	SCN-0.5	SCN-1	SCN-2	SCN
FWHM (°)	1.42	0.820	1.09	1.13	1.15	1.25
d (nm)	0.3225	0.3214	0.3211	0.3167	0.3164	0.3148

Table S2. The surface atomic percentages of C, N and S elements measured by XPS over GCN, CCN, SCN-0.5, SCN-1, and SCN. C1, C2 and C3 are related to graphitic carbon, sp^2-bonded carbon in the aromatic ring (N=C-N) and sp^3-bonded carbon in -C≡N groups, respectively, as displayed in Figure S4.

samples	C(at%)[a]			N(at%)	O(at%)	K(at%)	S(at%)	C/N	C/S
GCN	59.44			39.14	1.43	/	/	1.09	/
	C1(at%)	C2(at%)	C3(at%)						
	24.09	/	75.91						
CCN	55.21			22.15	6.61	16.03	/	1.18	/
	C1(at%)	C2(at%)	C3(at%)						
	52.52	12.68	34.8						
SCN-0.5	54.19			21.9	7.62	16.13	0.15	1.17	171.37
	C1(at%)	C2(at%)	C3(at%)						
	52.57	11.39	36.04						
SCN-1	55.67			22.67	7.08	14.02	0.56	1.22	49.33
	C1(at%)	C2(at%)	C3(at%)						
	50.38	9.93	39.69						
SCN-2	55.20			25.11	4.92	13.9	0.83	1.21	36.49
	C1(at%)	C2(at%)	C3(at%)						
	45.14	9.54	45.32						
SCN	57.14			18.16	8.71	14.39	1.6	1.41	16.03
	C1(at%)	C2(at%)	C3(at%)						
	55.13	18.04	26.83						

a, at% is the atomic percentage;

b, C:N atomic ratio is calculated by C:N=(C×(C2+C3)):N; C:S atomic ratio is calculated by C:S=(C×(C2+C3)):S, which could exclude the inevitable graphitic carbon (C1) originated from surrounding or contaminants.

Table S3. Photocatalytic CO_2 reduction performances of previously reported GCN-based photocatalysts without transition-metal and noble-metal modification.

Photocatalyst	Light source	Condition	CO reaction rate ($\mu mol \cdot g^{-1} \cdot h^{-1}$)	CO selectivity	Ref.
SCN-0.5	**300 W Xenon lamp, $\lambda > 420$ nm**	**gas-solid, water**	**16.5**	**95%**	**This work**
KP/CN-2	300 W Xenon lamp, $\lambda > 420$ nm	gas-solid, water	11.7	66.86%	[6]
K/S@CN-0.5	10 W Vlight lamp	gas-liquid-solid, KOH solution	16.3	78.07%	[7]
Vc-OCN_{15}	300W Xenon lamp, $\lambda > 400$ nm	gas-solid, water	13.7	~100%	[8]
BCN-1	420 nm–780 nm	gas-liquid-solid, water	13.9	92.3%	[9]
0.1K-AUCN	1 sun simulated sunlight, Xenon lamp	gas-solid, water	10.0	52.6%	[10]
Rh2/HCNS-Nv	300 W Xenon lamp	gas-solid, water	5.2	26.7%	[11]
E-CN	300 W Xenon lamp, $\lambda > 420$ nm	gas-solid, water	47.08	81%	[12]
CNSK+5%	300 W Xenon lamp	gas-solid, water	5.05	90.9%	[13]
Nv-rich-CN	300 W xenon lamp	gas-liquid-solid, water	6.6	97%	[14]
15%RGO/H-CN	300 W Xenon lamp, 400-800 nm	gas-solid, water	1.79	63.3%	[15]

References:

[1] a) G. Zhang, Y. Xu, D. Yan, C. He, Y. Li, X. Ren, P. Zhang, H. Mi, *ACS Catal.* **2021**, *11*, 6995-7005; b) Z. A. Lan, G. Zhang, X. Chen, Y. Zhang, K. A. I. Zhang, X. Wang, *Angew. Chem. Int. Ed.* **2019**, *58*, 10236-10240.

[2] L. M. Azofra, D. R. MacFarlane, C. Sun, *Phys. Chem. Chem. Phys.* **2016**, *18*, 18507-18514.

[3] G. Li, J. Han, H. Wang, X. Zhu, Q. Ge, *ACS Catal.* **2015**, *5*, 2009-2016.

[4] L. Jiang, K. Wang, X. Wu, G. Zhang, S. Yin, *ACS Appl. Mater. Interfaces* **2019**, *11*, 26898-26908.

[5] S. Yu, J. Li, Y. Zhang, M. Li, F. Dong, T. Zhang, H. Huang, *Nano Energy* **2018**, *50*, 383-392.

[6] M. Chen, M. Guo, M. Zhai, J. Xu, L. Wang, *J. of CO Util.* **2023**, *68*, 102392.

[7] J. M. Z. Liu, M. Hong, R. Sun, *ACS Catal.* **2023**, *13*, 2106−2117.

[8] J. Li, C. He, J. Wang, X. Gu, Z. Zhang, H. Li, M. Li, L. Wang, S. Wu, J. Zhang, *Green Chem.* **2023**, *25*, 8826-8837.

[9] X. Zeng, H. Chen, X. He, H. Zhang, W. Fang, X. Du, W. Li, Z. Huang, L. Zhao, *Environ. Res.* **2022**, *207*, 112178.

[10] Z. Sun, S. Wang, Q. Li, M. Lyu, T. Butburee, B. Luo, H. Wang, J. M. T. A. Fischer, C. Zhang, Z. Wu, L. Wang, *Adv. Sustainable Syst.* **2017**, *1*, 1700003.

[11] X. Ma, Q. Chen, C. Han, S. Zhou, Z. Li, J. Liu, F. Hu, J. Wang, N. Wang, Y. Zhu, J. Zhu, *Adv. Funct. Mater.* **2023**, *34*, 2307733.

[12] D. Chen, Z. Wang, J. Fu, J. Zhang, K. Dai, *Sci. China Mater.* **2024**, *67*, 541-549.

[13] R. Fang, Z. Yang, Z. C. Kadirova, Z. He, Z. Wang, J. Ran, L. Zhang, *Appl. Surf. Sci.* **2022**, *598*, 153848.

[14] F. Li, X. Yue, D. Zhang, J. Fan, Q. Xiang, *Appl. Catal. B Environ.* **2021**, *292*, 120179.

[15] Y. Liu, J. Shang, T. Zhu, *J. Mater. Sci. Technol.* **2024**, *176*, 36-47.